JACS
JOURNAL OF THE AMERICAN CHEMICAL SOCIETY
Article
pubs.acs.org/JACS

Electric Field Keeps Chromophore Planar and Produces High Yield Fluorescence in Green Fluorescent Protein

Jae Woo Park[†,‡] and Young Min Rhee*[,†,‡]

[†]Center for Self-assembly and Complexity, Institute for Basic Science (IBS), Pohang 37673, Korea
[‡]Department of Chemistry, Pohang University of Science and Technology (POSTECH), Pohang 37673, Korea

Supporting Information

ABSTRACT: The green fluorescent protein and its designed variants fluoresce efficiently. Because the isolated chromophore is not fluorescent in a practical sense, it is apparent that the protein environment plays a crucial role in its efficiency. Because of various obstacles in studying excited state dynamics of complex systems, however, the detailed mechanism of this efficiency enhancement is not yet clearly elucidated. Here, by adopting excited state nonadiabatic molecular dynamics simulations together with an interpolated quantum chemical potential model of the chromophore, we find that the strong electric field from the protein matrix contributes dominantly to the motional restriction of the chromophore. The delay in twisting motion subsequently obstructs the nonradiative decay that competes with fluorescence, leading naturally to an enhancement in light-emitting efficiency. Surprisingly, steric constraints make only a minor contribution to these aspects. Through residue specific analyses, we identify a group of key residues that control the excited state behavior. Testing a series of mutant GFPs with different brightnesses also supports the view regarding the importance of protein electrostatics. Our findings may provide a useful guide toward designing new fluorescent chemical systems in the future.

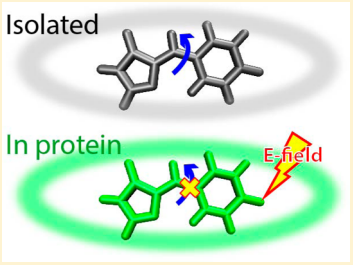

1. INTRODUCTION

The green fluorescent protein (GFP) is well-known for its high fluorescence efficiency. For example, the quantum yield of the wild-type *Aequorea victoria* GFP (*av*GFP)[1,2] is near to unity (0.79).[3,4] Indeed, such an efficiency is likely one of the most important aspects that has made this system quite useful. Thus, over the course of designing new mutants in the past few decades, researchers have considered the fluorescence quantum yield as an important criterion[1−14] and have repeatedly reported its enhancement[10−12] or reduction.[13,14] In this sense, understanding fundamental reasons behind the efficiency will be crucial for further developing new fluorescent proteins and other related photophysical systems.

Naturally, nonradiative decay, which is often associated with a geometric distortion in the chromophore, is a process that majorly competes with fluorescence.[3,15,16] In the case of *av*GFP, it is known that slowing chromophore twist is linked with fluorescence enhancement.[3,9,15] In fact, its isolated chromophore in solution without any motional restraints[16] twists very fast and does not fluoresce in a practical sense.[2,8,9,17−21] At first glance, the efficiency in the protein scaffold[1−4,6] may seem natural as the protein environment will sterically restrain the chromophore motion.[3,18,19] Namely, the barrel that contains the chromophore in GFP provides a crowded environment (Figure 1), and the chromophore twist will not be feasible as it will likely induce substantial structural rearrangements with an energetic penalty. On the other hand, there have been proposals that electrostatics may play a vital role in the fluorescence efficiency[3,21−23] based on quantum chemical observations that external electric field can severely affect chromophore energetics. Furthermore, it has been reported that photophysics of other systems could be modified with electrostatics, for example, photoactive yellow protein chromophore,[24] modified GFP chromophores,[25] and other photoisomerizing small organic molecules.[20,21] In fact, whether *sterics* or *electrostatics* dominates GFP efficiency in terms of slowing the chromophore twist has not yet been clearly elucidated.[19,20,26] This is likely because determining how the complex protein environment actually hinders the chromophore motion is not a trivial task.

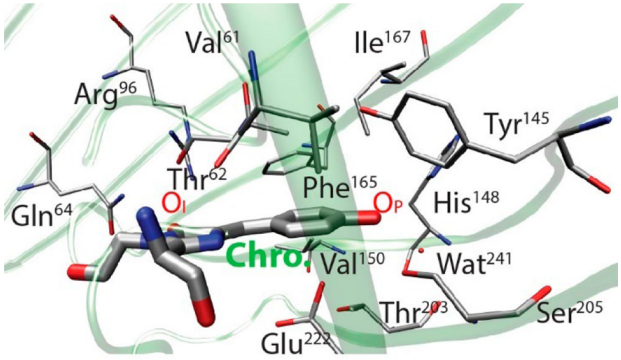

Figure 1. Chromophore environment in *av*GFP represented by residue alignments near the chromophore from the crystallographic structure (PDB ID: 1GFL).

Received: July 2, 2016
Published: September 23, 2016

DOI: 10.1021/jacs.6b06833
J. Am. Chem. Soc. 2016, 138, 13619−13629

In this paper, we investigate the origin of the fluorescence enhancement in GFP with nonadiabatic molecular dynamics (MD) simulations. By computationally modifying the electrostatic interactions between the chromophore and its environment, we reveal that the nonuniform electrostatic arrangement around the chromophore actually plays a dominant role in slowing the chromophore twist in *av*GFP. We find that even the bare chromophore in vacuum without any environmental steric constraints becomes highly fluorescent if the three-dimensional protein electric field is copied to the vacuum space. In particular, the interplay between the geometry-dependent charge transfer inside the chromophore and the protein electric field appears to be important for restraining the chromophore motion.[3] We further test our proposition by performing simulations of a series of GFP mutants with diverse quantum yields and show that the electrostatics is consistently important in reproducing experimentally observed fluorescence efficiencies. We also discuss the supporting role of steric interactions from the protein matrix with regard to preserving the protein electrostatic profile. Future prospects are also discussed as concluding remarks.

2. METHODS: OVERVIEW

To help readers understand how we reached our conclusions, we will provide here a very brief overview of our methodologies. More elaborate and comprehensive descriptions can be found in Computational Details with references to relevant literature.

In estimating the excited state lifetime of any given system, we conducted nonadiabatic molecular dynamics simulations through Landau–Zener (LZ) surface hopping with derivative coupling.[27−31] For this, the ground state (S_0) ensemble was first generated with S_0 equilibrium simulations. By assuming vertical transitions, the geometries and velocities from this ensemble were adopted as the initial conditions of subsequent excited state (S_1) simulations. During the S_1 simulations, at each trajectory integration step, nonradiative hopping to the S_0 state was attempted. Because multiple trajectories were simulated in this manner, the surviving population in the S_1 state as a function of time could be straightforwardly obtained and further utilized toward the lifetime estimation. The chromophore intramolecular potential energies and their couplings were previously constructed[32,33] with our diabatic interpolation scheme[34] based on a data set collected at the perturbatively corrected state-averaged complete active space level of theory, SA3-CAS(4,3)-PT2/6-31G(d).[35] The data set contained energy and derivative information at 1500 chromophore conformations and covered a wide range of configurational space.[32] The environment that surrounded the chromophore was described with the conventional molecular mechanics model. The chromophore–environment interaction was handled by adopting the interpolation mechanics/molecular mechanics (IM/MM) approach.[32,36−38] Indeed, IM/MM aims to follow the accuracy of the more demanding quantum mechanics/molecular mechanics (QM/MM) at a much reduced computational cost.[32] This approach models the interactions between the IM and the MM regions based on Coulomb and Lennard-Jones potentials together with linked hydrogen atoms over covalently bonded interfaces. The atomic partial charges of the chromophore were generated with our diabatic population matrix formalism[39] based on natural population analyses (NPA)[40] of the electron distributions in multiple electronic states. This formalism can properly describe charge distributions in multiple electronic states at diverse chromophore geometries and was tested favorably for the GFP chromophore in comparison to QM/MM calculations.[32,39] Furthermore, see Text S1 for its good correspondence to the restrained electrostatic potential (RESP)[41] charges. Even though our IM/MM scheme does not include a term for describing chromophore polarization by an external electric field, our previous study indicates that it reproduces the excited state population decay pattern quite well compared to that of QM/MM with an intrinsically polarizable chromophore.[39]

3. RESULTS AND DISCUSSION

Electrostatics and Excited State Lifetime. From our simulations of *av*GFP (Figure 2a), the nonradiative lifetime of

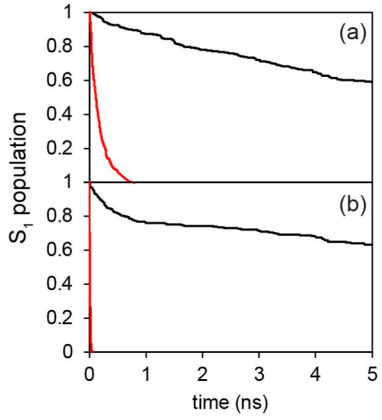

Figure 2. Nonradiative excited state decays in *av*GFP. (a) Simulated S_1 population decay patterns from *av*GFP: black, with natural setting; red, after nullifying chromophore–protein electrostatic interactions. (b) Simulated S_1 population decay patterns from bare chromophore: black, with 3D-ESP; red, without 3D-ESP.

the S_1 state was estimated to be longer than 8 ns. Indeed, this is comparable to the experimental estimation of 15 ns.[6] (See Text S2 for the extraction of the pure nonradiative lifetime from available experimental data.) To separate out the contribution by the electrostatics toward slowing the twist, we conducted another set of simulations in an equivalent manner but after nullifying atomic partial charges of the chromophore. With this setting, the nonradiative S_1 lifetime was estimated to be ∼0.2 ns (Figure 2a). Because the decay was fast without electrostatic interactions, we can infer that the Coulombic interactions between the chromophore and its environment may indeed play a dominant role in slowing nonadiabatic decay associated with the chromophore twist. However, it is not fully conclusive at this stage yet because nullifying the atomic charges of the chromophore may disrupt the structural arrangements with its neighboring protein residues. Indeed, from actual trajectories, we observed that hydrogen bonds and electrostatic contacts between the chromophore and its surrounding residues were sometimes disrupted. Thus, one may argue that electrostatics might actually be affecting the twisting dynamics through the chromophore–protein steric contacts, and the electrostatic effect would only be indirect.

To eliminate such ambiguity, we pursued a strategy that can truly isolate the electrostatic effects from the steric ones. This was achieved by replicating the nonuniform three-dimensional (3D) electrostatic potential (ESP) map from the initial protein conformation and then performing a new set of simulations for

DOI: 10.1021/jacs.6b06833
J. Am. Chem. Soc. 2016, 138, 13619−13629

the bare chromophore with the field from the ESP. From these gas phase simulations with the replicated 3D-ESP, the majority of the chromophore population still lasted in the excited state over 5 ns (Figure 2b). Indeed, a biexponential fit of the decay pattern provided a dominant component with a decay time constant over 10 ns. This shows that the electrostatics alone in the gas phase without any help from sterically contacting interactions can extend the excited lifetime similarly to that of the protein environment. Overall, we can conclusively infer that the electric field generated by the protein environment indeed dominates in extending the excited state lifetime and also in restricting the chromophore motion. We also note that the hydrogen bonds between the chromophore and its environment could be at least partly described with the replicated ESP because the electrostatic effects from O−H or N−H dipoles were present in 3D-ESPs.

Roles of Protein ESP in Modifying Energetics. What aspect of the ESP is so effective for slowing nonradiative transitions? As mentioned above, the nonradiative transitions in *av*GFP are frequently accompanied by chromophore twists. There are two twisting courses available, which are often referred to as the imidazolinone (*I*-) and the phenoxy (*P*-) pathways. (Of course, concurrent combinations of both are also possible.) When the molecule twists in the S_1 state from a planar geometry through these pathways, it becomes more stable in terms of energy, and often, the twists are considered to be barrierless for an isolated chromophore in vacuo or in solution.[2,17] Because a longer time was needed for the chromophore to twist with the replicated ESP, it is natural to imagine that the energetics along the twisting pathway was significantly altered. Thus, we first inspected the energy modifications with ESP by sequentially distorting the chromophore geometry around two corresponding twisting angles: τ and φ (Figure 3a). The energy modifications are pictorially presented in Figure 3b, and it shows that twisting away from planarity indeed drives the chromophore uphill in total potential with the replicated ESP. We also note that the S_1-S_0 energy gaps at *P*-twisted geometries are wider with the ESP, which will further impede the nonadiabatic transitions.

Now, let us investigate the residue-specific roles of the protein in modifying the energetics by focusing on groups that are close to the chromophore unit. Among the neighboring residues, those that would contact the chromophore phenolate ring (Ph) along the *P*-pathway were collected, and the 3D-ESP map originating from them was constructed. For succinctness, hereafter this group will be referred to as the "near-Ph group". Because the highly electrophilic chromophore oxygen atoms would importantly participate in shaping the electrostatic interactions, the residues near the phenolate oxygen atom (O_P) were also collected as the "near-O_P group". Likewise, residues that would exert stabilizing ESP on the imidazolinone oxygen atom (O_I) were additionally collected to form the "near-O_I group". The residues included in these groups can be found in Table 1.

The potential energy modifications by these groups are displayed in Figure 3c. One can easily see that the energy shift by the near-O_P group dominates, whereas the effect from the near-Ph group is very minor. Adding the near-O_I group to the near-O_P group slightly decreased the potential change at the 90-degree twist along the *P*-pathway. Excited state population decay patterns agreed well with this order. As presented in Figure 3d, nonadiabatic simulations with the 3D-ESP from the near-Ph group exhibited extremely fast decays mostly through

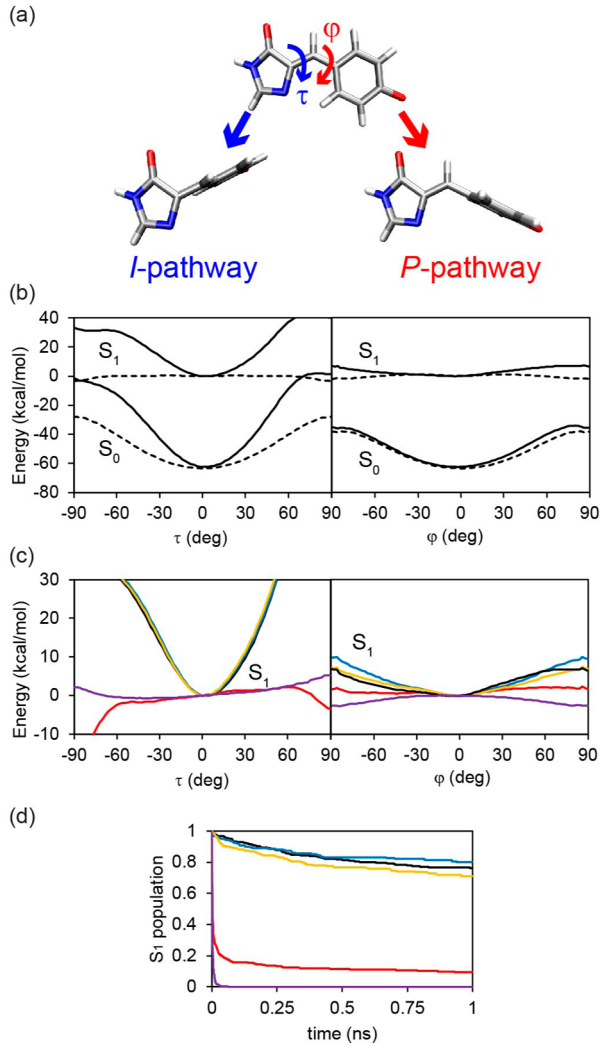

Figure 3. Electrostatic modifications of chromophore energetics and photodynamics. (a) Two twisting pathways and their associated dihedral angles. (b) S_0 and S_1 state energies along the *I*-pathway (left) and the *P*-pathway (right) twists. Solid lines show energies with 3D-ESP whereas dashed lines show data in vacuum without 3D-ESP. Energies were measured by twisting τ or φ angle from the Franck−Condon geometry. The S_1 energy at $\tau = \varphi = 0$ was adopted as the zero reference. (c) S_1 potential energies with ESP effects from the near-Ph group (red), the near-O_P group (blue), the near-O_I group (purple), and the near-O_P plus the near-O_I groups (yellow). The potential with ESP from the whole protein (black) is also displayed for comparison. (d) Population decay patterns with the group-specific ESP with the color coding as listed in (c).

Table 1. List of Chromophore-Neighboring Groups and Their Member Residues

group	member residues[a]
near-Ph	Val[61], Thr[62], Ser[205], Glu[222]
near-O_P	Tyr[145], His[148], Thr[203], Wat[241]
near-O_I	Gln[94], Arg[96]

[a]Residue numbering follows the indexing in the 1GFL PDB file.

the *I*-pathway. With the ESP from the near-O_P group, the decay lifetime was already comparable to the one computed with the whole protein. In contrast to the near-Ph group case, with the near-O_P group ESP the decays took place through the *P*-pathway. This contrast is quite understandable as twisting

DOI: 10.1021/jacs.6b06833
J. Am. Chem. Soc. 2016, 138, 13619−13629

around the *I*-pathway with the near-O_P ESP will be severely penalized with a steep potential barrier as shown in the left panel of Figure 3c.

Chromophore Conformations. Figure 4 presents the distributions of the (φ, τ) dihedral angles in the excited state

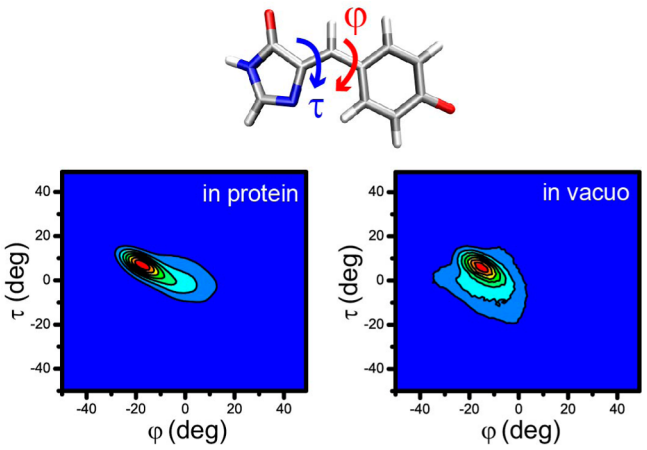

Figure 4. Two dimensional distributions of the two major twisting angles of the chromophore in the protein (left) and in vacuo with 3D-ESP (right).

before hopping, obtained from both the protein and the 3D-ESP simulations. The overall features of the two distributions match relatively well, suggesting that the chromophore travels in similar conformational spaces in the two situations. Interestingly, in the protein, the two angles vary with a slightly negative correlation. This is in line with a previous molecular simulation result with freely twisting chromophore in the protein matrix.[42] In any case, this figure shows that the chromophore mostly stayed close to planarity in the excited state. The chromophore traveled around this planar geometry for some time before twisting in a sudden manner and then decayed nonadiabatically into the ground state (Figure S1).

When we inspected the conformations at actual hopping events with the protein, we observed that the majority (~75%) were distorted with $|\varphi| > 70$ deg through the *P*-pathway. The angle τ was also displaced but to a lesser extent of ~15 deg, again in a negatively correlated manner to φ. The larger contribution by the *P*-pathway is in agreement with an earlier report based on multiple spawning nonadiabatic simulations[15] and can be easily understood by the smaller electrostatic energy penalty on that pathway shown in Figure 3b. Thus, from 3D-ESP simulations, not surprisingly more than 95% of hopping conformations displayed similar characteristics with $|\varphi| > 70$ deg with τ up to ~15 deg.

One outstanding difference between the protein and the 3D-ESP simulations was the fact that a small fraction (~15%) of trajectories hopped down with $|\tau| > 45$ deg from the protein simulations but not from the 3D-ESP simulations. We believe the difference arose from the lack of side chain flexibilities in the 3D-ESP model. Namely, when the chromophore happens to twist with a large $|\tau|$, the protein side chains may adjust to a region with lower electrostatic and/or steric energy penalty. The 3D-ESP model does not have that capability as the ESP maps are fixed to their initial forms throughout the simulations.

In addition, we observed that when $|\tau|$ was large at the hopping point, $|\varphi|$ was rather small (at most ~20 deg). In fact, we did not observe any case where both $|\varphi|$ and $|\tau|$ were larger than 45 deg at hopping. Thus, a hula twist with simultaneously large distortions around the two angles did not appear to participate importantly in our case. This is in agreement with previous multireference ab initio calculations in the gas phase or in implicit solvent[3,18,23,43] but is in contrast to the result from other semiempirical calculations.[44] From both protein simulations without electrostatics and bare chromophore simulations without 3D-ESP, *P*- and *I*-pathway twists were almost equally probable but their concurrent involvement was again not observed.[43]

Chromophore Charge Relocation and Twist Hindrance. With the results discussed above, a natural question one may ask is how twisting around the *P*-pathway is electrostatically affected by the residues in the near-O_P group. Namely, because such twisting will not displace the O_P atom of the chromophore in any meaningful manner, the distances between the O_P atom and the near-O_P group residues would be nearly invariant to that twist. Thus, one might expect that electrostatic aspects would change only marginally. In answering this, one important consideration is the fact that this position-conserving condition of the *P*-pathway twist[45] does not guarantee a dipole-conserving condition. With the *av*GFP chromophore, a twist in the S_1 adiabatic state is heavily linked with charge relocation inside it,[3,39] and the phenolate part becomes less negatively charged with the twist around the angle φ (Figure 5a). This will surely decrease the stabilization by the near-O_P residues, and this destabilization will be the main reason for the motional hindrance. This interplay between the charge relocation and the electrostatic environment is in

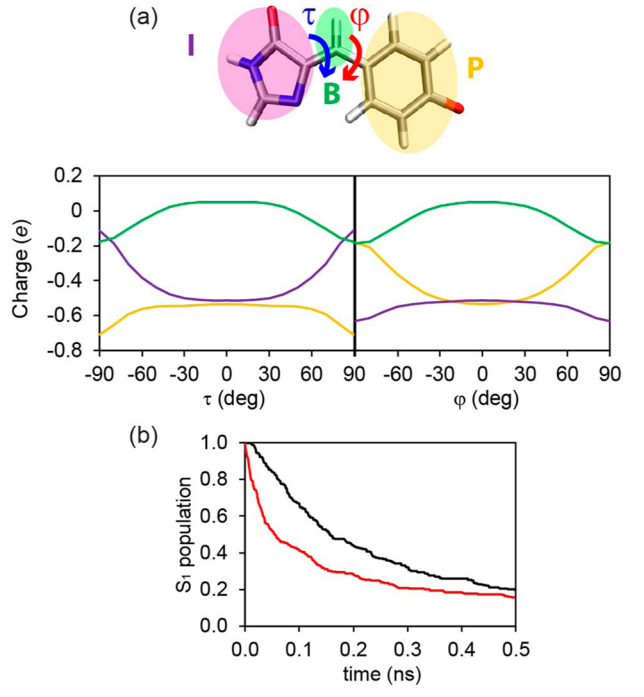

Figure 5. Chromophore charge transfer and its effect on nonradiative decay. (a) Charge contents of the phenolate (yellow), bridge (green), and imidazolinone (violet) moieties in the S_1 state with respect to the two twisting angles. (b) Population decay patterns without chromophore charge migration from the actual protein simulations (black) and the gas phase 3D-ESP simulations (red). The charge migration capability of the chromophore could be eliminated by fixing the chromophore atomic partial charges to their values at the planar geometry.

DOI: 10.1021/jacs.6b06833
J. Am. Chem. Soc. 2016, 138, 13619−13629

line with a previous suggestion based on chromophore electronic structure.[3,23] Indeed, we designed our chromophore model to be capable of describing such geometry-dependent charge relocation with the diabatic and state-specific atomic charge matrices.[39]

To confirm the importance of the geometry-dependent charge relocation, we performed an additional set of simulations after intentionally eliminating this capability. This was achieved by fixing the atomic partial charges to those at the planar geometry in the S_1 state. With this, the nonadiabatic decay lifetime became noticeably shorter regardless of the types of ESP from the environment (Figure 5b). Therefore, we can conclude that the interplay between the electric field from the protein scaffold and the charge transfer in the chromophore is the most important for improving the fluorescence efficiency in *av*GFP. The ESP shape shown in Figure 6 also supports this

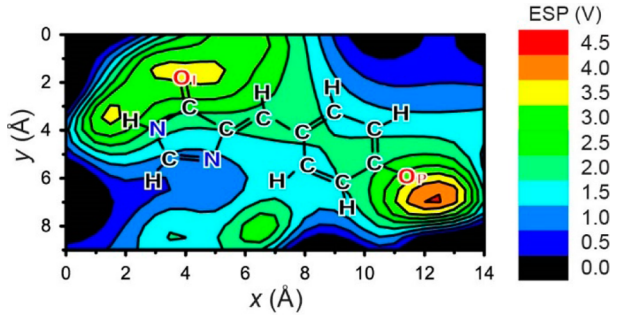

Figure 6. ESP map near the chromophore in *av*GFP based on the crystallographic structure.

argument. The C−O_P bond is located in a place with a large electric field (over 100 MV/cm at the O_P position with an ∼70 MV/cm component along the bond direction) and any motion that induces charge transfer against this field will be greatly hindered. It is also notable that the ESP shape around the O_P atom remains well-conserved regardless of the value of the φ angle (Figure S2). Because a fraction of the charge flows into the imidazolinone ring, the near-O_I residues would somewhat facilitate the twist. However, the effect was actually very small, as displayed in Figure 3d, because the electric field strength at the O_I position along the C−O_I bond direction was only ∼35 MV/cm. In addition, the magnitude of partial charge that migrated into the O_I atom was smaller than the flow out from O_P. The overall aspect of this electrostatic hindrance is pictorially summarized in Figure 7 together with three-dimensional representations of the interpolated potential energy surfaces with and without the 3D-ESP as functions of the key torsion angle φ and length r_p of the bond that bears the torsion. (The definition of r_p is also found in the figure.)

Tests with Other Mutants. Up to this point, we have shown that the electrostatic arrangement near the chromophore plays a dominant role in enhancing fluorescence of *av*GFP. Because our interpolated potential model[32] can be applied to other GFP mutants if they emit with an anionic chromophore,[33] we can additionally test whether the ESP is consistently important in those mutants. Indeed, such consistency will further support our view with more generality. Therefore, we have employed bright $T^{203}V$, semibright $H^{148}G/S^{65}T$, and dark REACh1 mutants to simulate them in both protein and 3D-ESP environments. These mutants were chosen because they cover a wide range of experimentally measured

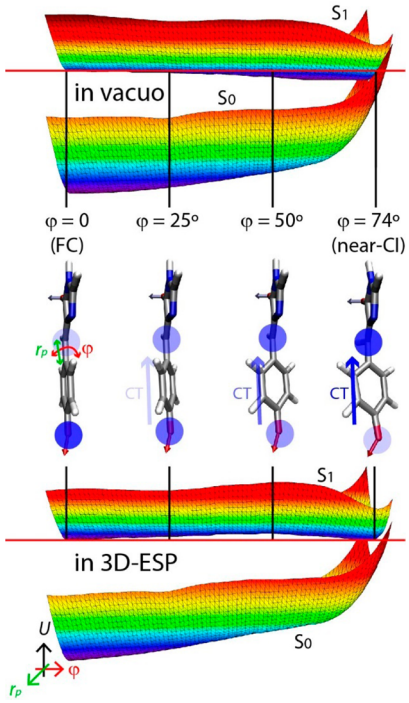

Figure 7. Schematic illustration of the electrostatic hindrance on chromophore twist in GFP. Along the C−O_P bond, the electric field strength is ∼70 MV/cm (red arrows, pointing to the opposite directions of field vectors). As the chromophore twists from the Franck−Condon structure (FC) into a near conical intersection geometry (near-CI; a point where the ground and excited state become nearly degenerate), −0.08 *e* of charge migrates away from the O_P atom toward the imidazolinone ring (blue arrows) against the field direction. As a consequence, the energetically downhill twist of the chromophore in vacuo toward the near-CI point (top) becomes an uphill transition (bottom). The potential energy surfaces were quantitatively drawn with interpolation. See Text S3 for more details on the surface drawing.

quantum yields (Table 2). The simulated nonadiabatic decay patterns are shown in Figure 8 together with the time scale

Table 2. List of GFP Mutants Adopted in This Work

name	mutation[a]	quantum yield[b]
$T^{203}V$	Thr^{203} → Val	0.75[4]
$H^{148}G/S^{65}T$	His^{148} → Gly	0.43[100]
	Ser^{65} → Thr	
REACh1	Ser^{65} → Gly	0.01[13]
	Val^{68} → Leu	
	Ser^{72} → Ala	
	Tyr^{145} → Trp	
	Thr^{203} → Tyr	

[a]In comparison to *av*GFP. [b]Experimental values with their refs.

comparisons of their nonradiative decays.[46] We can see that the experimental trends are satisfactorily reproduced from both protein and 3D-ESP simulations. This clearly supports our view that electrostatics dominates in deciding fluorescence lifetimes and quantum yields. In addition, the good correlation of decay times against experimental values shown in the inset of Figure 8a provide a hint as to the reliability of our IM/MM model.

For the specific protein forms, in the case of $T^{203}V$ we did not observe a large disturbance in the ESP shape because Thr^{203}

DOI: 10.1021/jacs.6b06833
J. Am. Chem. Soc. 2016, 138, 13619−13629

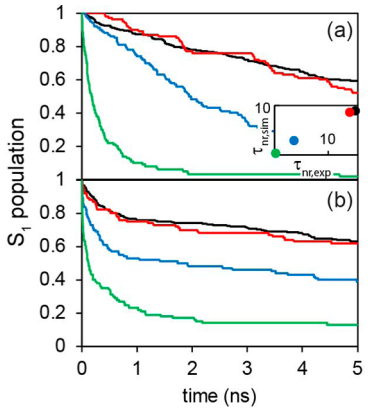

Figure 8. Simulated excited state decays from different GFP forms. (a) S_1 population decay patterns from the whole protein simulations with *av*GFP (black), $T^{203}V$ (red), $H^{148}G/S^{65}T$ (blue), and REACh1 (green). (b) Matching decay patterns from the 3D-ESP bare chromophore simulations with the same color coding as in (a). The inset displays the comparison between the experimental (horizontal) and simulated (vertical) nonradiative lifetimes. The experimental lifetimes were estimated as in Text S2, and the simulation numbers were derived from single exponential fits.[43]

in *av*GFP was somewhat farther from O_P than the other residues in the near-O_P group, and thus, its electrostatic effect was limited. In addition, when we inspected the ESP contour shape by the near-O_P group with and without Thr^{203}, we did not find any large difference. Thus, a slow nonradiative decay as in *av*GFP is quite well explained with our interpretation with electrostatics. In addition, our previous simulations with another mutant involving Thr^{203} ($T^{203}Y$) in its protein environment also generated a similarly slow nonradiative decay.[33] For $H^{148}G/S^{65}T$, because His^{148} exerts a large electrostatic effect to the chromophore and even forms a hydrogen bond with the O_P atom,[47] it was surprising that its replacement with glycine induced only a small change in the population decay pattern (Figure 8). We could explain this puzzling aspect after inspecting conformations in its equilibrium ensemble. Upon visual inspection, we observed that one water molecule flew into the space originally taken by the histidine side chain and formed a hydrogen bond with O_P. The location of this water molecule was not as highly conserved as the crystal water in the proton transfer wire (Wat^{241}) due to the lack of a second hydrogen-bonding partner in the protein. However, it could still partially take the role His^{148} was playing, and even the ESP shapes were similar. This case of the $H^{148}G/S^{65}T$ mutant clearly suggests the caution that we have to take when considering GFP mutants. Because of the crowded nature in the protein barrel, replacing a residue near the chromophore will always induce a chain of events that may appear counterintuitive when only the replaced residue is considered. Indeed, the darkest REACh1 mutant should be handled with such caution. In this mutant, in the vicinity of the chromophore, Tyr^{145} is replaced with bulkier tryptophan in addition to the $T^{203}Y$ mutation. Not surprisingly, from our equilibrating simulations we observed that the chromophore was somewhat displaced with this change. Likely owing to this dislocation, the electrostatic environment of the O_I atom was changed even though the mutated residues were rather far from O_I in the *av*GFP crystal structure.[5] (The shortest atom-to-atom distance is 5.4 Å.) Surely, this case emphasizes that electrostatic modulations arise as a combined result of many individual changes. In this sense, it will be appropriate to consider that REACh1 characters are influenced by a synergistic combination of its key mutations $Y^{145}W$ and $T^{203}Y$.

Despite the complex nature of these changes, a simplified explanation can still help us to obtain useful insights. For the varyious dynamics of the different GFP forms considered here, a simple reasoning could again be attained by considering the ESP map around the chromophore. Figure 9 shows the average ESP maps from the four adopted protein forms. As explained previously, a portion of negative charge migrates from the phenolate ring toward the imidazolinone ring upon the chromophore twist. Thus, if the ESP around O_P is lowered (more negative), twisting will be promoted, and the fluorescence efficiency will subsequently drop. For a similar reason, the efficiency will drop if the ESP around O_I is raised. This is precisely what is revealed in Figure 9. The ESP features, especially around the O_P and O_I atoms for $T^{203}V$, match quite well with *av*GFP, and the quantum yields of the two are quite close. In comparison, the ESP around O_I is raised in $H^{148}G/$

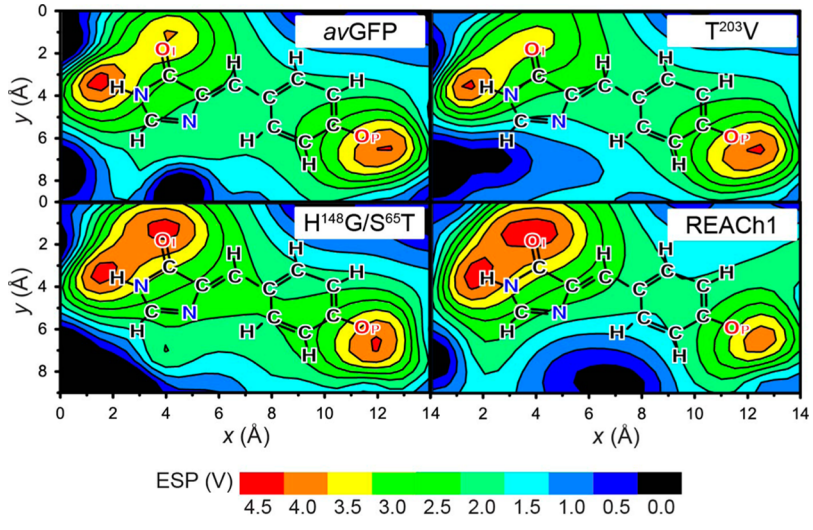

Figure 9. Average ESP maps near the chromophore in different GFP forms. The averages were taken by using the snapshots of equilibrium ensembles after aligning chromophore structures.

DOI: 10.1021/jacs.6b06833
J. Am. Chem. Soc. 2016, 138, 13619−13629

$S^{65}T$, and its quantum yield is smaller. REACh1 has both lower O_P and higher O_I potentials, and its quantum yield is very low. Of course, this argument in Figure 9 is a simplification as it does not consider other detailed aspects, such as the variations of ESP for different ensemble members. Therefore, drawing quantitative analysis from the figure alone is not ideal. However, it is still intriguing that this simple electrostatic analysis can successfully explain the trends of all tested GFP variants. In addition, we stress again that our 3D-ESP simulations in the gas phase correctly reproduced the features of the whole protein simulations for all of the mutants. Clearly, this is strong evidence of the importance of electrostatics in restraining chromophore motion.

Furthermore, it is intriguing to note that twist hindrance and spectral shift show independent behaviors, even though both are strongly affected by electrostatics. For example, the twisting behavior of $T^{203}V$ was very similar to the behavior of *av*GFP as discussed above. However, from our simulations we could observe that this mutation induced ∼0.03 eV red shift in the emission (Figure S3). An earlier experiment also observed nearly the same amount of shift.[4] Another highly fluorescent $T^{203}Y$ mutant (quantum yield of ∼0.83) also displayed a noticeable red shift in its emission.[4,33] In fact, one should expect to see independent responses because the two aspects are affected differently by electrostatics. Namely, the emission color is changed by the S_1-S_0 gap energy modulation, whereas the twist hindrance is affected by the S_1 state PES shape modulation, especially along the φ-twisting degree of freedom.

Role of Steric Contacts. We additionally note that steric contacts still have their own roles in improving fluorescence. For example, Figure 2a demonstrates that eliminating electrostatics but keeping steric effects could extend the excited state lifetime to ∼0.2 ns. The three mutants listed in Table 2 also displayed similar lifetimes under the same influence of steric conditions (Figure S4). Indeed, this value coincides quite well with the 0.2−0.4 ns S_1 lifetime of the bare chromophore in solution below freezing temperatures.[16] Thus, we can infer that the crowded environment in the protein barrel likely restrains the chromophore motion similarly to a viscous environment in a supercooled liquid. However, the extent that it extends the fluorescence lifetime is limited compared to the electrostatic effect. Nonetheless, we have to admit that nonpolar residues near the chromophore are still important for maintaining the positions of key polar residues. For example, when we tested a spatial mutant by computationally replacing nonpolar residues (Val^{150}, Phe^{165}, and Ile^{167}) into alanine, we observed that the chromophore storing pocket structure was disrupted during the equilibration stage. This disruption severely distorted the ESP shape, and the barrier toward the chromophore twist disappeared. Consequently, the nonradiative decay from the S_1 state was very fast in this case (Figure S5). Therefore, we can infer that the nonpolar residues still contribute to maintaining the structural feature in the barrel and to shaping the ESP in the correct manner.

Additionally, steric contacts will be important for cooling a vibrationally hot chromophore right after light absorption. Without this intermolecular vibrational energy transfer, the chromophore S_1-S_0 surface crossing region will be more frequently visited. Thus, not surprisingly, when we did not employ the temperature controlling algorithm in our bare chromophore simulations the chromophore did not stay in the excited state as long.

4. CONCLUDING REMARKS

In summary, we have shown that the efficient fluorescence of *av*GFP is mainly achieved by the electric field shaped by the protein environment.[48] The chromophore has a tendency to twist in the excited state, and the twisting motion induces charge relocation across the chromophore. Because the electrostatic setting by the protein disfavors this charge relocation, the twisting motion is effectively hindered. Furthermore, because the twisting motion is nearly a prerequisite condition for the nonradiative decay that competes with fluorescence, this electrostatic hindrance on the chromophore motion consequently enhances the fluorescence efficiency. The dominance of electrostatics was confirmed by adopting bare chromophore simulations with the three-dimensional electrostatic potential map copied from the protein matrix. Simulations of GFP mutants with varying brightness also supported our argument on the importance of electrostatics toward enhancing fluorescence. Steric effects from chromophore-contacting residues appeared to play a limited role toward the enhancement, but they were still important in terms of preserving the electrostatic arrangements in an intact form.

In a sense, it is remarkable that the protein electrostatics in *av*GFP match the chromophore characteristics so well in terms of this enhancement. Then again, it is known that protein electrostatics can be shaped toward improving protein function, such as enzymatic reactions.[49,50] Perhaps nature has utilized the same tool for evolving fluorescent proteins. We note that electrostatics was reported to be similarly important in another photoprotein system,[24] and thus we can hypothesize that the aspect may be quite general. In this sense, further testing our conclusion with more GFP mutants, for example, the ones with neutral chromophore with different electrostatic characters,[4,11,12,37,51] will be an interesting task for future investigations. In addition, as designing better fluorescing systems is gaining continued attention from many researchers,[52] and as the involved fluorophores often have geometry-dependent charge relocating characters in their emitting states,[53,54] employing a strategy that is similar to what GFP does might find good utility in related future studies. Indeed, understanding fluorescence processes is a rather complicated task because it requires us to explore multiple electronic states that are often connected by multiple pathways.[20,21,24] Of course, the environment can affect these multiple aspects in widely varying manners.[21,24] Thus, we anticipate that simulations with new, advanced techniques will surely have the potential to provide useful insights for understanding such complex events.

5. COMPUTATIONAL DETAILS

Potential Model: Interpolated Diabatic Hamiltonian. In conventional MD simulations, atomic movements are calculated by solving Newton's equations of motion.[55,56] The most expensive task in MD simulations is generally calculating the potential U and its gradient. The computational effort required for U becomes even more severe when U is obtained with quantum chemical methods on the fly, especially toward describing electronically excited molecules. Potential energy surface interpolation was suggested as an alternative to this direct dynamics approach.[36,37,57−70] In the interpolation approach, a data set is first constructed with N molecular geometries together with their energies and energy derivatives before performing production level simulations. The potential energy at an arbitrary molecular geometry $\mathbf{X}$ is given as a weighted sum of the Taylor-expanded potential energies (U_i) from each point $\mathbf{X}_i$ in the data set,

DOI: 10.1021/jacs.6b06833
J. Am. Chem. Soc. 2016, 138, 13619−13629

$$U(\mathbf{X}) = \sum_{i=1}^{N} w_i(\mathbf{X};\, \mathbf{X}_i) U_i(\mathbf{X};\, \mathbf{X}_i) \tag{1}$$

This method was initially developed for describing gas phase chemistry[59−70] and then extended to investigating condensed phase systems,[36] such as following protein photodynamics.[37]

To simulate nonadiabatic dynamics of electronically excited molecules, one needs to evaluate the potential energies and their couplings of multiple electronic states.[20,27−29,71−75] In this case, for avoiding difficulties of handling singularities in the derivative coupling vectors,[74−76] interpolating diabatic potential energy matrices becomes more desirable.[76−78] The diabatic potential $\mathbf{D}$ at an arbitrary geometry $\mathbf{X}$ is interpolated similarly to eq 1,

$$\mathbf{D}(\mathbf{X}) = \sum_{i=1}^{N} w_i(\mathbf{X};\, \mathbf{X}_i) \mathbf{D}_i(\mathbf{X};\, \mathbf{X}_i) \tag{2}$$

This is readiabatized on the fly as

$$\mathbf{U} = \mathbf{R}\mathbf{D}\mathbf{R}^{\mathrm{T}} \tag{3}$$

with the adiabatic-to-diabatic transformation matrix $\mathbf{R}$.[32,34,74−76] The derivative coupling vector elements between a pair of adiabatic states k and l along the Cartesian coordinate X_m can be computed with the relationship

$$(\mathbf{F}_{kl})_m = -\frac{\mathbf{e}_k^{\mathrm{T}}(\partial \mathbf{D}/\partial X_m)\mathbf{e}_l}{U_k - U_l} \tag{4}$$

where $\mathbf{e}_k$ and $\mathbf{e}_l$ are the corresponding column vectors of $\mathbf{R}$.[32,34,76]

In the condensed phase simulations using the interpolated diabatic Hamiltonian, the electrostatic interactions can also be described based on diabatic states. With this, it becomes possible to describe geometry-dependent charge migration in the chromophore on each adiabatic potential energy surface. Operationally, the electrostatic interactions between the chromophore and its environment are described within the atomic partial charge approximation as

$$\mathbf{D}_{\mathrm{coul}} = \sum_{a}^{N_a} \sum_{A}^{N_A} \frac{q_A}{|\mathbf{X}_A - \mathbf{X}_a|} \mathbf{q}_a \tag{5}$$

where N_a and N_A are the numbers of atoms in the chromophore and in its environment, respectively.[39] The diabatic atomic partial charge matrix of an atom a is defined as $\mathbf{q}_a$ based on natural population analyses. Of course, q_A is the molecular mechanics charge on an environmental atom A. Curious readers are referred to refs 32, 34, and 39 for more details.

Nonadiabatic Trajectory Simulations. As mentioned in section 2, the nonadiabatic events were described with the Landau−Zener (LZ)-type surface hopping algorithm.[27−31] This algorithm yields population decay patterns that are similar to the ones from the more popular fewest switches surface hopping (FSSH) algorithm[72,73,79] but allows one to use longer time steps for a significant reduction in the computational cost.[29,39] The transition probability is calculated as

$$P = \exp\left(-\frac{\pi}{4}\frac{U_k - U_j}{\hbar \mathbf{F}_{kj}\cdot\mathbf{v}}\right) \tag{6}$$

where $\mathbf{F}_{kj}$ is the derivative coupling vector between states k and j, $\mathbf{v}$ is a velocity vector of the trajectory, and U_k and U_j are the potential energies of the two adiabatic states. In our simulations, when this probability was larger than 0.5 and the gap energy between two states was smaller than 25 kJ/mol, the trajectory was forced to hop to the ground state.[27,39] Although the LZ hopping approach may not be a quantitatively perfect method toward obtaining kinetic data, because we adopted the same approach consistently throughout all kinetics simulations, their comparisons will surely be meaningful.

We also confirmed that this LZ hopping generated consistent results in comparison to decoherence-corrected FSSH by comparing both methods with bare chromophore simulations with the 3D-ESP map. This comparison is shown in Figure S6. In FSSH, the quantum amplitude of an electronic state C_k is propagated with the relationship

$$i\hbar\frac{\mathrm{d}C_k}{\mathrm{d}t} = U_k C_k - i\hbar \sum_{n}^{\#\mathrm{states}} C_n \mathbf{F}_{kn}\cdot\mathbf{v} \tag{7}$$

At each trajectory integration step, a uniform random number is generated, and if a quantity g_{kj} defined as

$$g_{kj} = \frac{-2\int_t^{t+\Delta t} \mathrm{Re}(C_k C_j^*)\mathbf{F}_{kj}\cdot\mathbf{v}\mathrm{d}\tau}{\mathrm{Re}(C_k C_j^*)} \tag{8}$$

is larger than that random number, the trajectory hop occurs from state k to j. Total energy conservation of the system is forced by adjusting velocity component along $\mathbf{F}_{kj}$ when the hop occurs. In this work, the overcoherence problem of FSSH[73,79−85] was corrected with a simple collapse scheme.[79,82,83] This scheme scales the quantum amplitudes of all electronic states so that the decoherence effect can appear in a long time limit. Specifically, when a trajectory is running on state k after deciding a hop, C_j with $j \neq k$ was scaled at every integration step of time Δt as

$$C_j' = C_j \exp(-\Delta t/t_{jk}) \tag{9}$$

with a demixing time coefficient t_{jk},

$$t_{jk} = \frac{\hbar}{|U_j - U_k|}\left(1 + \frac{\alpha}{E_{\mathrm{K}}}\right) \tag{10}$$

Of course, C_k was also scaled to compensate for the change in C_j. Here, E_{K} is the kinetic energy, and α is an empirical parameter with a suggested value of 0.1 hartree.[79,82,83] This decoherence correction was reported to be capable of amending the FSSH kinetics with regard to the number of trajectories that survive in the excited state.[82]

Protein Simulation Details. Interpolated mechanics/molecular mechanics (IM/MM) simulations with the diabatic Hamiltonian[32] was employed toward the MD simulations of the whole protein. The GROMACS 4.0.7 program package[86] with in-house external libraries for the diabatic Hamiltonian interpolation and the surface hopping algorithms was used for all simulations with the protein. Toward the combined IM/MM scheme, the *av*GFP model chromophore, *para*-hydroxybenzylidene-imidazolinone (*p*HBI), was treated as the IM region with two linked atoms replacing the connecting points to the protein backbone as in our previous studies.[33,37,39] The same diabatic Hamiltonian interpolation data set adopted in our previous study[32,33] was again employed. This set contained 1500 geometrical points whose energy and gradient information was calculated with the perturbatively corrected state-averaged complete active space level of theory, SA3-CAS(4,3)-PT2/6-31G(d), supplemented by Hessian data from SA3-CAS(4,3)/6-31G(d) level calculations. The rest of the protein besides the chromophore was considered as the MM region and was treated with the AMBER99SB force field.[87,88] Water molecules were treated explicitly with the rigid three-point model TIP3P.[89] To avoid erratic behaviors far from the interpolated regions of the chromophore conformational space, a stabilizer function[36] adopted from AMBER99SB force field[87,88] with a damping constant s = 0.02 was utilized. The dispersive and electrostatic interactions were treated via force shifting with 10 Å cutoffs. The electrostatic interactions between the chromophore and its environment were calculated according to eq 5, by employing the diabatic population matrix.[39] The dispersive interactions were treated with the conventional Lennard-Jones potential with custom-optimized parameters for the chromophore.[32,90] The integration time step size was 2 fs for these simulations. All bonds involving hydrogen atoms were constrained with the LINCS algorithm.[91]

The simulations were based on the crystallographic structure of *av*GFP (PDB ID: 1GFL).[5] Protonation states of its titratable residues were determined with PROPKA 2.0[92] except for Glu^{222}, to which a proton was specifically added to properly model the protonation state after the excited state proton transfer (ESPT).[7,8,93] This geometry was

DOI: 10.1021/jacs.6b06833
J. Am. Chem. Soc. 2016, 138, 13619−13629

used for generating the representative electric potential map shown in Figure 6. Before production simulations, this geometry was further energy-minimized with the steepest descent method[94] and was then soaked in a cubic box of water with side lengths of 60 Å. This solvated system was again energy-minimized and was then thermally equilibrated. For equilibration, a random initial velocity corresponding to a temperature of 300 K was assigned and a 500 ps MD simulation was performed with Berendsen's weak coupling thermostat and barostat algorithms[95] that targeted 300 K and 1 bar conditions. Following this, an additional equilibration run of 15 ns duration at the same temperature and pressure was performed using the Nosé–Hoover thermostat[96] and the Parrinello–Rahman barostat.[97] After this, a 5 ns production simulation was performed to generate an ensemble of 250 equilibrated snapshots separated with 20 ps intervals. We assumed that this ensemble would represent the situation after the Franck–Condon transition well and used it as the initial conditions of the actual nonadiabatic surface hopping simulations. Each nonadiabatic trajectory was continued until the chromophore hopped down to the electronic ground state or up to a maximum duration of 10 ns. In the case of the protein simulations with nullified electrostatics, as the majority of trajectories hopped down much earlier, we only propagated up to 1 ns.

The same protocol was employed for conducting the mutant simulations except that the total number of nonadiabatic trajectories was reduced to 100 for computational efficiency. A mutant structure was generated by replacing relevant side chains from the equilibrated *av*GFP structure and by then performing a re-equilibrating simulation over a 5 ns period. (See Figure S7 for the mutation-related structural robustness check.) This was followed by a 2 ns simulation toward obtaining 100 initial conformations for the excited state trajectories. Overall, the aggregate simulation time for the excited state trajectories reached multiple microseconds.

Bare Chromophore Simulation Details. As explained in section 3, we also simulated bare chromophore in vacuo after mimicking the 3D-ESP around the chromophore. This can be trivially achieved by replacing eq 5 with

$$\mathbf{D}'_{\mathrm{coul}} = \sum_a \mathbf{q}_a V(\mathbf{X}_a) \tag{11}$$

once the 3D-ESP at any arbitrary point $\mathbf{X}$ is given as $V(\mathbf{X})$. Again, $\mathbf{q}_a$ is the diabatic partial charge matrix of an atom a in the chromophore at a geometrical point $\mathbf{X}_a$. In MD simulations, of course, the first-order derivative of V (namely, the electric field) is also needed. To obtain smoothly defined values, we employed tricubic spline interpolation[98] of V and its derivatives. This required the ESP and its derivative components (V; $\partial V/\partial x$, $\partial V/\partial y$, $\partial V/\partial z$; $\partial^2 V/\partial x\partial y$, $\partial^2 V/\partial y\partial z$, $\partial^2 V/\partial z\partial x$; $\partial^3 V/\partial x\partial y\partial z$) at predefined 3D grid points.

Positions of these grid points were determined as follows. Any given initial geometry of the chromophore was first aligned on the *xy*-plane as in Figure 6. As displayed in the same figure, the *x*-axis was defined as the line connecting the N atom originating from glycine (namely, the leftmost N atom) and the C_γ atom originating from tyrosine (namely, the C atom on the phenolate ring that connects to the bridging group). The *z*-axis was defined with the normal vector that was perpendicular to the phenolate (tyrosyl) ring of the chromophore after projecting out a component along the *x*-axis. The origin was defined such that the leftmost N atom was located at $(x, y, z) = (3, 4, 6)$ Å. Cartesian grid points were filled within a rectangular box defined by vertex points of (0, 0, 0) Å and (14, 9, 12) Å. The grid spacing was 0.5 Å such that there were 29 × 19 × 25 grid points in the box. Simply put, the gridded box was designed to cover a volume generated by scanning the rectangular plane in Figure 6 with ±6 Å depth. This box was large enough to contain the chromophore even after a full rotation along the *P*-pathway.

On these grid points, the ESPs and their derivatives for the spline interpolation were computed by considering the atomic partial charges of the MM atoms within the cutoff distance from these grid points. The MM atoms were either from the protein residues or from the water molecule participating in the proton wire around the chromophore. Of course, for consistency, the same force-shifted Coulomb function that was adopted in the protein simulations was employed for generating the ESPs, except for one modification. Because the ESP function has a singularity at $r \approx 0$, if a grid point is too close to an MM atom, the ESP will become singular. The same singularity exists in regular protein simulations but does not cause trouble because the Lennard-Jones potential will repel an atom pair well outside the singular regime. In our bare chromophore simulations with ESP maps, there were no such repelling interactions from the MM atoms, and the singularities in the 3D-ESP would unphysically generate too high or too low energy state when any of the IM atoms hit the singular regime. To avoid this issue, we modeled the MM atoms as permeable Gaussian-like charged spheres[99] with a decay factor of $\beta = 1.0$ Å^{-1} in $\rho(r) \sim e^{-\beta^2 r^2}$. Even though the choice of the charge shape is somewhat arbitrary, it describes physically unimportant regions in a reasonable way. Furthermore, we verified that the chromophore excited state decay patterns were rather insensitive to the choice of the smeared charge shape.

With the ESP maps thus generated, we performed nonadiabatic MD simulations after restraining the atoms on the imidazolinone ring with a force constant of $k = 10000$ kJ mol^{-1} Å^{-2}. The restraints were imposed in such a way that the chromophore could not unphysically drift or flip in space. To this end, the two linked H atoms were restrained in 3D, and four additional atoms that were one and two bonds away from the linked H atoms were restrained on the chromophore molecular plane. The four planar restraints were implemented by first aligning the chromophore on the *xy*-plane and then adding *z*-directional restraining potentials. We confirmed that these restraints did not affect the excited state lifetimes to any meaningful degree throughout the simulations by conducting two sets of comparing simulations in the gas phase. First, without 3D-ESP, we observed that the population decays were fast whether we imposed the chromophore restraints or not (Figure S8a). Next, with 3D-ESP, we checked that the decays were similarly slow even when the restraining potential was weakened by a factor of 2 (Figure S8b).

For all simulations, the initial geometries and the atomic velocities of the chromophore were the same as in the matching protein simulations. Here, the integration time step was 0.5 fs, and no constraints were imposed. The same interpolated potential was used for describing the chromophore with a stabilizer function[36] damped by $s = 0.02$. The trajectories were integrated up to 5 ns. Bare chromophore simulations with ESPs either from selected residue groups in *av*GFP or from the three GFP mutants were performed in the same manner. In all these bare chromophore simulations, there was no need to perform pressure adjustments. However, thermalizing the chromophore was still important as intermolecular vibrational energy transfer can participate importantly to condensed-phase excited-state dynamics. Therefore, we applied Berendsen's temperature coupling scheme with a coupling time constant of $\tau_c = 10$ ps. Applying stronger or weaker coupling with different τ_c had only marginal effects on the excited-state decaying patterns (Figure S9).

■ ASSOCIATED CONTENT

Supporting Information

The Supporting Information is available free of charge on the ACS Publications website at DOI: 10.1021/jacs.6b06833.

Supporting text with the correspondence between NPA and RESP charges, our estimation scheme of pure nonradiative lifetimes, strategy for drawing the 3D potential shape shown in Figure 7, and discussion on Stark shift by protein electric field; supporting figures that show twisting angle variations in time, additional ESP maps, spectral shift of $T^{203}V$, the role of steric contacts, a comparison between LZ and FSSH results, structural robustness of our mutant models, and the validations on using restraints and temperature coupling for bare chromophore simulations (PDF)

DOI: 10.1021/jacs.6b06833
J. Am. Chem. Soc. 2016, 138, 13619–13629

AUTHOR INFORMATION

Corresponding Author

*ymrhee@postech.ac.kr

Notes

The authors declare no competing financial interest.

ACKNOWLEDGMENTS

Y.M.R. gratefully acknowledges stimulating and fruitful correspondences with Steven Boxer and Todd Martínez (Stanford University). This work was supported by the Institute for Basic Science (IBS) in Korea.

REFERENCES

(1) van Thor, J. J. *Chem. Soc. Rev.* **2009**, *38*, 2935−2950.
(2) Meech, S. R. *Chem. Soc. Rev.* **2009**, *38*, 2922−2934.
(3) Martin, M. E.; Negri, F.; Olivucci, M. *J. Am. Chem. Soc.* **2004**, *126*, 5452−5464.
(4) Jung, G.; Wiehler, J.; Zumbusch, A. *Biophys. J.* **2005**, *88*, 1932−1947.
(5) Yang, F.; Moss, L. G.; Phillips, G. N., Jr. *Nat. Biotechnol.* **1996**, *14*, 1246−1251.
(6) Tsien, R. Y. *Annu. Rev. Biochem.* **1998**, *67*, 509−544.
(7) Chattoraj, M.; King, B. A.; Bublitz, G. U.; Boxer, S. G. *Proc. Natl. Acad. Sci. U. S. A.* **1996**, *93*, 8362−8367.
(8) Polyakov, I. V.; Grigorenko, B. L.; Epifanovsky, E. M.; Krylov, A. I.; Nemukhin, A. V. *J. Chem. Theory Comput.* **2010**, *6*, 2377−2387.
(9) Bravaya, K. B.; Grigorenko, B. L.; Nemukhin, A. V.; Krylov, A. I. *Acc. Chem. Res.* **2012**, *45*, 265−275.
(10) Mena, M. A.; Treynor, T. P.; Mayo, S. L.; Daugherty, P. S. *Nat. Biotechnol.* **2006**, *24*, 1569−1571.
(11) Ai, H.-W.; Shaner, N. C.; Cheng, Z.; Tsien, R. Y.; Campbell, R. E. *Biochemistry* **2007**, *46*, 5904−5910.
(12) Day, R. N.; Davidson, M. W. *Chem. Soc. Rev.* **2009**, *38*, 2887−2921.
(13) Ganesan, S.; Ameer-beg, S. M.; Ng, T. T. C.; Vojnovic, B.; Wouters, F. S. *Proc. Natl. Acad. Sci. U. S. A.* **2006**, *103*, 4089−4094.
(14) Kummer, A. D.; Kompa, C.; Lossau, H.; Pöllinger-Dammer, F.; Michel-Beyerle, M. E.; Silva, C. M.; Bylina, E. J.; Coleman, W. J.; Yang, M. M.; Youvan, D. C. *Chem. Phys.* **1998**, *237*, 183−193.
(15) Olsen, S.; Lamothe, K.; Martínez, T. J. *J. Am. Chem. Soc.* **2010**, *132*, 1192−1193.
(16) Kummer, A. D.; Kompa, C.; Niwa, H.; Hirano, T.; Kojima, S.; Michel-Beyerle, M. E. *J. Phys. Chem. B* **2002**, *106*, 7554−7559.
(17) Mandal, D.; Tahara, T.; Meech, S. R. *J. Phys. Chem. B* **2004**, *108*, 1102−1108.
(18) Jonasson, G.; Teuler, J.-M.; Vallverdu, G.; Mérola, F.; Ridard, J.; Lévy, B.; Demachy, I. *J. Chem. Theory Comput.* **2011**, *7*, 1990−1997.
(19) Addison, K.; Heisler, I. A.; Conyard, J.; Dixon, T.; Bulman Page, P. C.; Meech, S. R. *Faraday Discuss.* **2013**, *163*, 277−296.
(20) Virshup, A. M.; Punwong, C.; Pogorelov, T. V.; Lindquist, B. A.; Ko, C.; Martínez, T. J. *J. Phys. Chem. B* **2009**, *113*, 3280−3291.
(21) Martínez, T. J. *Acc. Chem. Res.* **2006**, *39*, 119−126.
(22) Martínez, T. J. *Faraday Discuss.* **2004**, *127*, 227−266.
(23) Altoe, P.; Bernardi, F.; Garavelli, M.; Orlandi, G.; Negri, F. *J. Am. Chem. Soc.* **2005**, *127*, 3952−3963.
(24) Ko, C.; Virshup, A. M.; Martínez, T. J. *Chem. Phys. Lett.* **2008**, *460*, 272−277.
(25) Cui, G.; Lan, Z.; Thiel, W. *J. Am. Chem. Soc.* **2012**, *134*, 1662−1672.
(26) Maddalo, S. L.; Zimmer, M. *Photochem. Photobiol.* **2006**, *82*, 367−372.
(27) Li, X.; Chung, L. W.; Mizuno, H.; Miyawaki, A.; Morokuma, K. *J. Phys. Chem. Lett.* **2010**, *1*, 3328−3333.
(28) Frutos, L. M.; Andruniów, T.; Santoro, F.; Ferré, N.; Olivucci, M. *Proc. Natl. Acad. Sci. U. S. A.* **2007**, *104*, 7764−7769.
(29) Boggio-Pasqua, M.; Burmeister, C. F.; Robb, M. A.; Groenhof, G. *Phys. Chem. Chem. Phys.* **2012**, *14*, 7912−7928.
(30) Zener, C. *Proc. R. Soc. London, Ser. A* **1932**, *137*, 696−702.
(31) Landau, L. D. *Phys. Z. Sowjetunion* **1932**, *2*, 46−51.
(32) Park, J. W.; Rhee, Y. M. *ChemPhysChem* **2014**, *15*, 3183−3193.
(33) Park, J. W.; Rhee, Y. M. *Phys. Chem. Chem. Phys.* **2016**, *18*, 3944−3954.
(34) Park, J. W.; Rhee, Y. M. *J. Chem. Phys.* **2014**, *140*, 164112.
(35) Celani, P.; Werner, H.-J. *J. Chem. Phys.* **2003**, *119*, 5044−5057.
(36) Park, J. W.; Kim, H. W.; Song, C.-I.; Rhee, Y. M. *J. Chem. Phys.* **2011**, *135*, 014107.
(37) Park, J. W.; Rhee, Y. M. *J. Phys. Chem. B* **2012**, *116*, 11137−11147.
(38) Kim, C. W.; Park, J. W.; Rhee, Y. M. *J. Phys. Chem. Lett.* **2015**, *6*, 2875−2880.
(39) Park, J. W.; Rhee, Y. M. *J. Chem. Theory Comput.* **2014**, *10*, 5238−5253.
(40) Reed, A. E.; Weinstock, R. B.; Weinhold, F. *J. Chem. Phys.* **1985**, *83*, 735−746.
(41) Bayly, C. I.; Cieplak, P.; Cornell, W. D.; Kollman, P. A. *J. Phys. Chem.* **1993**, *97*, 10269−10280.
(42) Megley, C. M.; Dickson, L. A.; Maddalo, S. L.; Chandler, G. J.; Zimmer, M. *J. Phys. Chem. B* **2009**, *113*, 302−308.
(43) Olsen, S.; Smith, S. C. *J. Am. Chem. Soc.* **2008**, *130*, 8677−8689.
(44) Weber, W.; Helms, V.; McCammon, A. J.; Langhoff, P. W. *Proc. Natl. Acad. Sci. U. S. A.* **1999**, *96*, 6177−6182.
(45) Baffour-Awuah, N. Y. A.; Zimmer, M. *Chem. Phys.* **2004**, *303*, 7−11.
(46) Of course, the single exponential fit used for generating lifetimes in Figure 8 will not be the best strategy for the given data shape but it will suffice for qualitative comparisons with experimental numbers.
(47) Wachter, R. M.; Elsliger, M.-A.; Kallio, K.; Hanson, G. T.; Remington, S. J. *Structure* **1998**, *6*, 1267−1277.
(48) Of course, the protein electric field also induces spectral shifts. For example, see (a) Drobizhev, M.; Tillo, S.; Makarov, N. S.; Hughes, T. E.; Rebane, A. *J. Phys. Chem. B* **2009**, *113*, 12860−12864. (b) Drobizhev, M.; Callis, P. R.; Nifosi, R.; Wicks, G.; Stoltzfus, C.; Barnett, L.; Hughes, T. E.; Sullivan, P.; Rebane, A. *Sci. Rep.* **2015**, *5*, 13223. (c) Slocum, J. D.; Webb, L. J. *J. Am. Chem. Soc.* **2016**, *138*, 6561−6570 and ref 33. For more discussion in this regard, see Text S4 in Supporting Information.
(49) Fried, S. D.; Bagchi, S.; Boxer, S. G. *Science* **2014**, *346*, 1510−1514.
(50) Warshel, A.; Sharma, P. K.; Kato, M.; Xiang, Y.; Liu, H.; Olsson, M. H. M. *Chem. Rev.* **2006**, *106*, 3210−3235.
(51) Zimmer, M. *Chem. Rev.* **2002**, *102*, 759−781.
(52) Hong, Y.; Lam, J. W. Y.; Tang, B. Z. *Chem. Soc. Rev.* **2011**, *40*, 5361−5388.
(53) Grabowski, Z. R.; Rotkiewicz, K.; Rettig, W. *Chem. Rev.* **2003**, *103*, 3899−4031.
(54) Singha, S.; Kim, D.; Roy, B.; Sambasivan, S.; Moon, H.; Rao, A. S.; Kim, J. Y.; Joo, T.; Park, J. W.; Rhee, Y. M.; Wang, T.; Kim, K. H.; Shin, Y. H.; Jung, J.; Ahn, K. H. *Chem. Sci.* **2015**, *6*, 4335−4342.
(55) Frenkel, D.; Smit, B. *Understanding Molecular Simulation*; Academic Press: London, 2002.
(56) Allen, M. P.; Tildesley, D. J. *Computer Simulation of Liquids*; Oxford University Press: Oxford, 1987.
(57) Evenhuis, C. R.; Collins, M. A. *J. Phys. Chem. A* **2009**, *113*, 3979−3987.
(58) Collins, M. A. *J. Chem. Phys.* **2007**, *127*, 024104.
(59) Moyano, G. E.; Pearson, D.; Collins, M. A. *J. Chem. Phys.* **2004**, *121*, 12396−12401.
(60) Moyano, G. E.; Collins, M. A. *J. Chem. Phys.* **2004**, *121*, 9769−9775.
(61) Rhee, Y. M. *J. Chem. Phys.* **2000**, *113*, 6021−6024.
(62) Collins, M. A.; Zhang, D. H. *J. Chem. Phys.* **1999**, *111*, 9924−9931.
(63) Bettens, R. P. A.; Hansen, T. A.; Collins, M. A. *J. Chem. Phys.* **1999**, *111*, 6322−6332.
(64) Thompson, K. C.; Jordan, M. J. T.; Collins, M. A. *J. Chem. Phys.* **1998**, *108*, 564−578.

DOI: 10.1021/jacs.6b06833
J. Am. Chem. Soc. 2016, 138, 13619−13629

(65) Thompson, K. C.; Jordan, M. J. T.; Collins, M. A. *J. Chem. Phys.* **1998**, *108*, 8302−8316.
(66) Jordan, M. J. T.; Collins, M. A. *J. Chem. Phys.* **1996**, *104*, 4600−4610.
(67) Nguyen, K. A.; Rossi, I.; Truhlar, D. G. *J. Chem. Phys.* **1995**, *103*, 5522−5530.
(68) Jordan, M. J. T.; Thompson, K. C.; Collins, M. A. *J. Chem. Phys.* **1995**, *103*, 9669−9675.
(69) Jordan, M. J. T.; Thompson, K. C.; Collins, M. A. *J. Chem. Phys.* **1995**, *102*, 5647−5657.
(70) Ischtwan, J.; Collins, M. A. *J. Chem. Phys.* **1994**, *100*, 8080−8088.
(71) Toniolo, A.; Olsen, S.; Manohar, L.; Martínez, T. J. *Faraday Discuss.* **2004**, *127*, 149−163.
(72) Hammes-Schiffer, S.; Tully, J. C. *J. Chem. Phys.* **1994**, *101*, 4657−4667.
(73) Tully, J. C. *J. Chem. Phys.* **1990**, *93*, 1061−1071.
(74) Pacher, T.; Cederbaum, L. S.; Köppel, H. *J. Chem. Phys.* **1988**, *89*, 7367−7381.
(75) Domcke, W.; Yarkony, D. R.; Köppel, H. *Conical Intersections: Theory, Computation and Experiment*; World Scientific: Singapore, 2004.
(76) Godsi, O.; Evenhuis, C. R.; Collins, M. A. *J. Chem. Phys.* **2006**, *125*, 104105.
(77) Evenhuis, C. R.; Martínez, T. J. *J. Chem. Phys.* **2011**, *135*, 224110.
(78) Evenhuis, C. R.; Collins, M. A. *J. Chem. Phys.* **2004**, *121*, 2515−2527.
(79) Barbatti, M. *WIRES Comput. Mol. Sci.* **2011**, *1*, 620−633.
(80) Bittner, E. R.; Rossky, P. J. *J. Chem. Phys.* **1995**, *103*, 8130−8143.
(81) Schwartz, B. J.; Bittner, E. R.; Prezhdo, O. V.; Rossky, P. J. *J. Chem. Phys.* **1996**, *104*, 5942−5955.
(82) Granucci, G.; Persico, M. *J. Chem. Phys.* **2007**, *126*, 134114.
(83) Zhu, C.; Nangia, S.; Jasper, A. W.; Truhlar, D. G. *J. Chem. Phys.* **2004**, *121*, 7658−7670.
(84) Subotnik, J. E.; Shenvi, N. *J. Chem. Phys.* **2011**, *134*, 024105.
(85) Bittner, E. R.; Rossky, P. J. *J. Chem. Phys.* **1997**, *107*, 8611−8618.
(86) Hess, B.; Kutzner, C.; van der Spoel, D.; Lindahl, E. *J. Chem. Theory Comput.* **2008**, *4*, 435−447.
(87) Hornak, V.; Abel, R.; Okur, A.; Strockbine, B.; Roitberg, A.; Simmerling, C. *Proteins: Struct., Funct., Genet.* **2006**, *65*, 712−725.
(88) Sorin, E. J.; Pande, V. S. *Biophys. J.* **2005**, *88*, 2472−2493.
(89) Jorgensen, W. L.; Chandrasekhar, J.; Madura, J. D.; Impey, R. W.; Klein, M. L. *J. Chem. Phys.* **1983**, *79*, 926−935.
(90) Song, C.-I.; Rhee, Y. M. *Int. J. Quantum Chem.* **2011**, *111*, 4091−4105.
(91) Hess, B.; Bekker, H.; Berendsen, H. J. C.; Fraaije, J. G. E. M. *J. Comput. Chem.* **1997**, *18*, 1463−1472.
(92) Bas, D. C.; Rogers, D. M.; Jensen, J. H. *Proteins: Struct., Funct., Genet.* **2008**, *73*, 765−783.
(93) Grigorenko, B. L.; Nemukhin, A. V.; Polyakov, I. V.; Morozov, D. I.; Krylov, A. I. *J. Am. Chem. Soc.* **2013**, *135*, 11541−11549.
(94) Fletcher, R. *Practical Methods of Optimization*; Wiley: New York, 1987.
(95) Berendsen, H. J. C.; Postma, J. P.; van Gunsteren, W. F.; Di Nola, A.; Haak, J. R. *J. Chem. Phys.* **1984**, *81*, 3684−3690.
(96) Nosé, S. *J. Chem. Phys.* **1984**, *81*, 511−519.
(97) Parrinello, M.; Rahman, A. *J. Appl. Phys.* **1981**, *52*, 7182−7190.
(98) Lekien, F.; Marsden, J. *Int. J. Numer. Meth. Engng.* **2005**, *63*, 455−471.
(99) Elking, D.; Darden, T.; Woods, R. J. *J. Comput. Chem.* **2007**, *28*, 1261−1274.
(100) Hanson, G. T.; McAnaney, T. B.; Park, E. S.; Rendell, M. E. P.; Yarbrough, D. K.; Chu, S.; Xi, L.; Boxer, S. G.; Montrose, M. H.; Remington, S. J. *Biochemistry* **2002**, *41*, 15477−15488.

DOI: 10.1021/jacs.6b06833
J. Am. Chem. Soc. 2016, 138, 13619−13629